Cell Reports

Article

Structures of the human Wilson disease copper transporter ATP7B

Graphical abstract

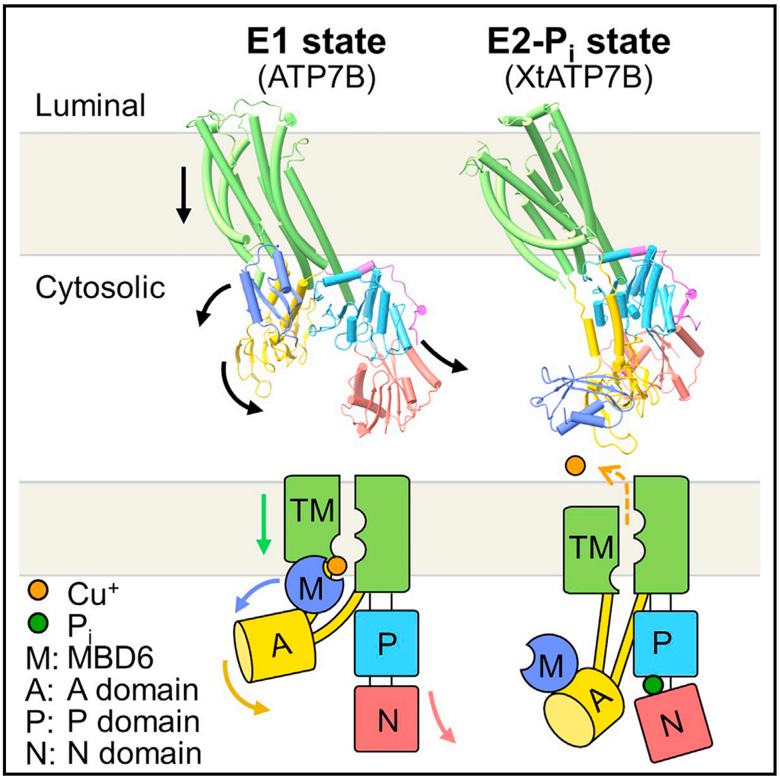

Highlights

- The cryo-EM structures of human ATP7B in the E1 state are determined
- The sixth metal-binding domain (MBD6) delivers Cu^+ to the transmembrane domain (TMD)
- The sulfur-containing residues in the TMD mark the copper transport pathway
- Comparisons with previous $E2\text{-}P_i$ structures reveal the copper transport model of ATP7B

Authors

Guo-Min Yang, Lingyi Xu, Rou-Min Wang, ..., Shan Wu, Jiangtao Guo, Zhi-Ying Wu

Correspondence

wushan91@hubu.edu.cn (S.W.),
jiangtaoguo@zju.edu.cn (J.G.),
zhiyingwu@zju.edu.cn (Z.-Y.W.)

In brief

The Wilson disease protein ATP7B is a P-type ATPase responsible for cellular copper transport. Yang et al. report human ATP7B cryo-EM structures, proposing the copper transport pathway and model, which contributes to the understanding of the molecular mechanisms of ATP7B and the development of potential treatments.

Yang et al., 2023, Cell Reports *42*, 112417
May 30, 2023 © 2023 The Author(s).
https://doi.org/10.1016/j.celrep.2023.112417

Cell Reports

CellPress
OPEN ACCESS

Article

Structures of the human Wilson disease copper transporter ATP7B

Guo-Min Yang,[1,11] Lingyi Xu,[2,11] Rou-Min Wang,[1] Xin Tao,[3] Zi-Wei Zheng,[1] Shenghai Chang,[4,5] Demin Ma,[2] Cheng Zhao,[2] Yi Dong,[1] Shan Wu,[3,*] Jiangtao Guo,[2,6,7,8,9,10,*] and Zhi-Ying Wu[1,9,10,12,*]
[1]Department of Medical Genetics and Center for Rare Diseases, and Department of Neurology in Second Affiliated Hospital, and Key Laboratory of Medical Neurobiology of Zhejiang Province, Zhejiang University School of Medicine, Hangzhou, Zhejiang 310009, China
[2]Department of Biophysics, and Department of Neurology of the Fourth Affiliated Hospital, Zhejiang University School of Medicine, Hangzhou, Zhejiang 310058, China
[3]State Key Laboratory of Biocatalysis and Enzyme Engineering, Hubei Collaborative Innovation Center for Green Transformation of Bio-Resources, Hubei Key Laboratory of Industrial Biotechnology, School of Life Sciences, Hubei University, Wuhan, Hubei 430062, China
[4]Department of Biophysics, and Department of Pathology of Sir Run Run Shaw Hospital, Zhejiang University School of Medicine, Hangzhou, Zhejiang 310058, China
[5]Center of Cryo Electron Microscopy, Zhejiang University School of Medicine, Hangzhou, Zhejiang 310058, China
[6]State Key Laboratory of Plant Physiology and Biochemistry, College of Life Sciences, Zhejiang University, Hangzhou, Zhejiang 310058, China
[7]Department of Cardiology, Key Laboratory of Cardiovascular Intervention and Regenerative Medicine of Zhejiang Province, Sir Run Run Shaw Hospital, Zhejiang University School of Medicine, Hangzhou, Zhejiang 310016, China
[8]Cancer Center, Zhejiang University, Hangzhou, Zhejiang 310058, China
[9]Liangzhu Laboratory, Zhejiang University Medical Center, 1369 West Wenyi Road, Hangzhou, Zhejiang 311121, China
[10]NHC and CAMS Key Laboratory of Medical Neurobiology, MOE Frontier Science Center for Brain Science and Brain-machine Integration, School of Brain Science and Brain Medicine, Zhejiang University, Hangzhou, Zhejiang 310016, China
[11]These authors contributed equally
[12]Lead contact
*Correspondence: wushan91@hubu.edu.cn (S.W.), jiangtaoguo@zju.edu.cn (J.G.), zhiyingwu@zju.edu.cn (Z.-Y.W.)

https://doi.org/10.1016/j.celrep.2023.112417

SUMMARY

The P-type ATPase ATP7B exports cytosolic copper and plays an essential role in the regulation of cellular copper homeostasis. Mutants of *ATP7B* cause Wilson disease (WD), an autosomal recessive disorder of copper metabolism. Here, we present cryoelectron microscopy (cryo-EM) structures of human ATP7B in the E1 state in the apo, the putative copper-bound, and the putative cisplatin-bound forms. In ATP7B, the N-terminal sixth metal-binding domain (MBD6) binds at the cytosolic copper entry site of the transmembrane domain (TMD), facilitating the delivery of copper from the MBD6 to the TMD. The sulfur-containing residues in the TMD of ATP7B mark the copper transport pathway. By comparing structures of the E1 state human ATP7B and E2-P$_i$ state frog ATP7B, we propose the ATP-driving copper transport model of ATP7B. These structures not only advance our understanding of the mechanisms of ATP7B-mediated copper export but can also guide the development of therapeutics for the treatment of WD.

INTRODUCTION

The human ATP-dependent copper exporter ATP7B holds a significant position in maintaining cellular copper homeostasis.[1,2] It transports intracellular copper in two ways. Usually, ATP7B is located in the *trans*-Golgi network and delivers copper into the Golgi for the biosynthesis of copper-containing enzymes (cuproenzymes). When the cytosolic copper concentration elevates, ATP7B traffics to cytosolic vesicles and enriches copper in vesicular compartments, facilitating copper excretion into bile along with the vesicle fusion.[3,4]

Dysfunction of ATP7B directly causes Wilson disease (WD), an autosomal recessive disorder of copper metabolism.[5,6] In patients with WD, defective copper export leads to the accumulation of copper in the liver first, and then with excess copper released into the circulation, other organs, particularly the brain, become affected.[5,7,8] Clinical manifestations can vary widely, including liver injury, neuropsychiatric disturbances, and Kayser-Fleischer (K-F) rings in the eyes.[9,10] Patients with WD require life-long therapy, and in some serious cases, liver transplantation is necessary.[11–13] Up to now, hundreds of pathogenic variants have been detected and experimentally explored in *ATP7B*,[14–16] but their pathogenesis and genotype-phenotype correlations still need further study.

ATP7B belongs to PIB-ATPases,[17] the heavy-metal pump family of the P-type ATPase.[18] Common to other P-type ATPases such as Ca^{2+}-ATPases and Na^+/K^+-ATPase,[19] ATP7B contains the transmembrane domain (TMD), the actuator (A) domain, the phosphorylation (P) domain, and the nucleotide-binding (N) domain. Based on the Albers-Post model,[20,21]

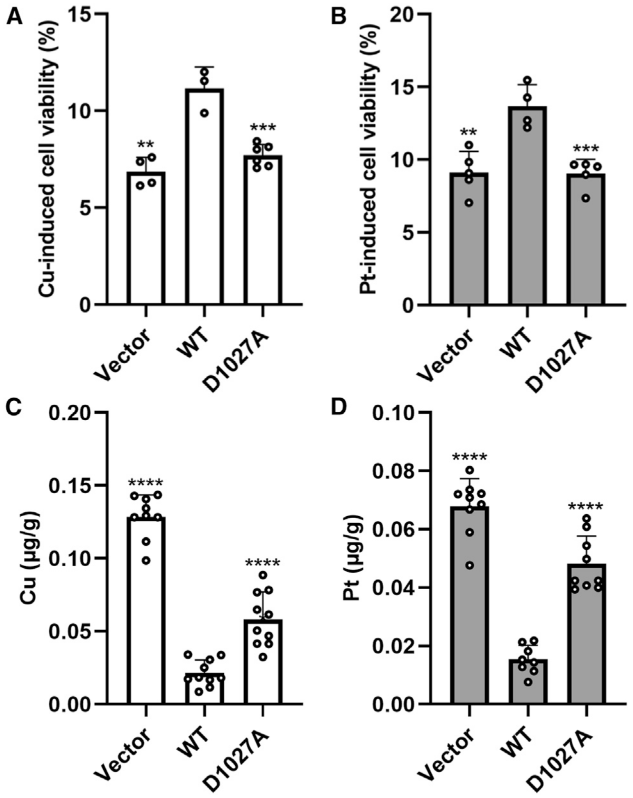

Figure 1. The copper and cisplatin transport activity of human ATP7B

(A and B) The effect of the empty plasmid vector, wild-type (WT) ATP7B, and the D1027A mutant on HEK293T cell viability after the treatment with 1 mM $CuCl_2$ or 100 μM cisplatin for 24 h. Data are expressed as mean ± SD ($n \geq 3$, $^{**}p < 0.01$, $^{***}p < 0.001$).

(C and D) The effect of the empty plasmid vector, WT ATP7B, and the D1027A mutant on HEK293T cellular metal accumulation after the treatment with 500 μM $CuCl_2$ or 100 μM cisplatin for 24 h. Data are expressed as mean ± SD ($n \geq 8$, $^{****}p < 0.0001$).

ATP7B transports Cu^+ across the membrane by isomerizing between the E1 and E2 conformational states, which display a high and low affinity for Cu^+, respectively. The translocation of Cu^+ is coupled to phosphorylation of an invariant Asp residue in the P domain and subsequent dephosphorylation.[18] The TMD of ATP7B consists of eight transmembrane helices where a typical CPC motif is directly involved in the Cu^+ binding.[22] Before the TMD, there are six unique metal-binding domains (MBDs) with identical CXXC motifs.[23] It has been experimentally shown that the fifth MBD (MBD5) and the MBD6 with a tight connecting loop are indispensable for the function of ATP7B, while MBD1–MBD4 with long and flexible linkers play a regulatory role.[24–26] Presumably, copper is delivered from a chaperone protein ATOX1 to several or all of MBDs,[27–29] and then the MBD5 and the MBD6 transfer copper to the TMD. Nevertheless, the exact route and regulation of copper translocation are unclear.

In addition, overexpression of ATP7B is relevant to resistance to several chemotherapeutic agents such as cisplatin in tumor cells.[30,31] To elucidate the phenomenon, some investigations have characterized that cisplatin can be chelated by the CXXC motifs of ATP7B MBDs[32,33] or may undergo an ATP-dependent transport similar to Cu^+ and become sequestrated into endolysosomal compartments.[34,35] To overcome this obstacle for cancer treatment, three biosafe drugs were identified to enhance cisplatin toxicity and simultaneously suppress the expression or trafficking of ATP7B, hence improving cisplatin efficacy.[36] Despite these findings, a better knowledge of the ATP7B relationship with cisplatin is eagerly desired.

Previously, structures of two ATP7B homologs in the E2-P_i state were reported. In 2011, the first high-resolution structure of the copper-transporting ATPase from *Legionella pneumophila* (LpCopA) was determined through X-ray crystallography in a copper-released E2-P_i state.[37] Very recently, the cryoelectron microscopy (cryo-EM) structure of ATP7B from *Xenopus tropicalis* (XtATP7B) was determined in a copper-free E2-P_i state.[38] These structures greatly advance our understanding of the overall architectures and molecular mechanisms of ATP7B proteins. To better unveil the mechanisms of ATP7B, herein we present the structures of human ATP7B in the E1 state in the apo form and in complex with putative copper or cisplatin. The structures, along with the metal transport assay, reveal the mechanisms of copper and cisplatin transport by ATP7B and provide the structural basis for the treatment of ATP7B-related WD and cisplatin resistance.

RESULTS

Functional characterization of human ATP7B

We utilized two *in vitro* methods to characterize the copper and cisplatin transport activity of human ATP7B. First, as both copper and cisplatin in excess are toxic to cells,[39,40] we measured the cell viability after the treatment of copper and cisplatin. Second, we directly quantified the cellular copper and platinum accumulation using inductively coupled plasma mass spectrometry (ICP-MS). The empty plasmid vector, wild-type (WT) ATP7B, and catalytically inactive mutant D1027A of ATP7B were transiently expressed in HEK293T cells. After the treatment with 1 mM $CuCl_2$ or 100 μM cisplatin for 24 h, severe cell damage occurred in all cells. Compared with the WT ATP7B group, cell injury in the empty vector and the D1027A mutant groups was even more serious (Figures 1A and 1B). This indicates that functionally active ATP7B protein can enhance copper and cisplatin tolerance of cells. Consistently, Cu and Pt levels in cells transfected with the empty vector and the D1027A mutant were higher than those with WT when they were exposed to 500 μM $CuCl_2$ or 100 μM cisplatin for 24 h (Figures 1C and 1D). These data together confirm the capability of WT ATP7B in copper and cisplatin excretion.

Structure determination and overall structure of ATP7B

Due to the low expression level of WT ATP7B in HEK293F cells for the structural study, we introduced three mutations at the active sites of ATP7B, namely C983S and C985S, the copper-binding site in the TMD, and D1027A, the phosphorylation site in the P domain. The combined mutations impaired the transport activity of ATP7B as indicated by the observation that HEK293T cells expressing the mutant showed increased metal accumulation and lower cell viability than those expressing WT ATP7B

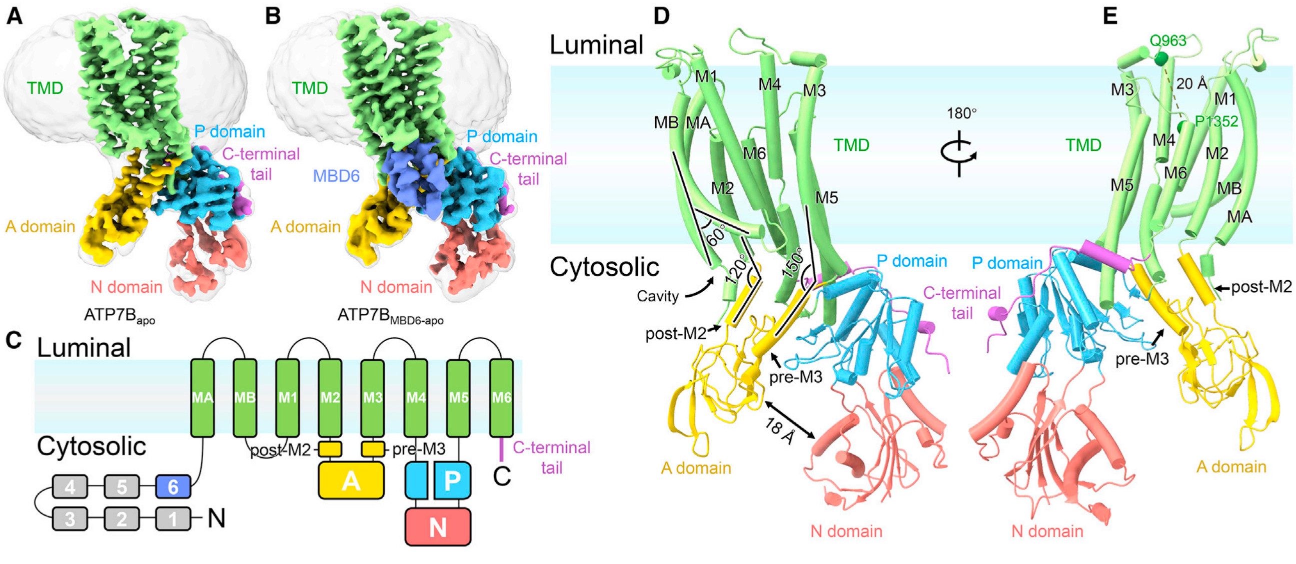

Figure 2. Overall structure of ATP7B

(A) 3D reconstruction of ATP7B$_{apo}$ with each domain individually colored.

(B) 3D reconstruction of ATP7B$_{MBD6\text{-}apo}$ with each domain individually colored.

(C) Topology diagram of ATP7B, with individual domains colored as in (A) and (B). MBDs 1–5 (gray); MBD6 (purple blue); TMD (green); post-M2 and pre-M3 linker (yellow); C-terminal tail (purple). A, A domain (yellow); P, P domain (blue); N, N domain (red).

(D) Cartoon representation of ATP7B$_{apo}$ in the same orientation as the map in (A). The angle shows the bending of MB and the turns formed by M2 and post-M2 and by pre-M3 and M3. The black double arrow shows the distance between the A domain and N domain.

(E) The transporters in (D) are rotated by 180° around the y axis. The dashed line shows the distance between Cα atoms of P1352 and Q963.

when exposed to copper or cisplatin (Figure S1). Nevertheless, this triple mutant of the full-length ATP7B exhibited a high expression level in HEK293F cells and a high homogeneity under the cryo conditions (Figures S2A and S2B). Using this protein sample, we determined the cryo-EM structure of apo ATP7B (ATP7B$_{apo}$) at 3.4 Å resolution (Figures 2A, S2A–S2F, and S4A–S4C; Table S1). In ATP7B$_{apo}$, the TMD, A domain, P domain, and N domain were unambiguously modeled, but none of the six MBDs were observed (Figure 2A). Because the chaperone protein ATOX1 delivers the copper to ATP7B,[27–29] we then co-expressed the full-length ATP7B triple mutant with ATOX1 and determined the cryo-EM structure of the ATP7B in the apo state in the presence of ATOX1 at 3.3 Å resolution (Figures 2B, S2G–S2L, and S4D–S4F; Table S1). The ATOX1 ratio was low in the complex sample as shown in the SDS-PAGE (Figure S2G), and no density corresponding to ATOX1 was identified in the map (Figure 2B). Instead, we were able to clearly resolve the MBD6 in the map (Figure 2B) and therefore named this structure ATP7B$_{MBD6\text{-}apo}$ (residues 562–1115 and 1144–1405). Using this sample, we also solved the ATP7B structures in the presence of copper (ATP7B$_{MBD6\text{-}Cu}$) or cisplatin (ATP7B$_{MBD6\text{-}Pt}$), both at 3.6 Å resolution (Figures S3A–S3J and S4G–S4H; Table S1). The four structures are essentially the same in the TMD, A, P, and N domains (Figures S5A–S5C).

As the ATP7B$_{apo}$ structure was determined in the absence of ATP, ADP, or the substrate copper, it is presumably in a substrate-free E1 state, which is consistent with the absence of nucleotide density in the ATP-/ADP-binding pocket between the N and P domains and ion density in the CPC motif of the TMD (Figures S4B and S4C). In addition, the E1 state is supported by conformations of all four domains, as analyzed below. This E1 state structure of ATP7B$_{apo}$ largely differs from previously reported structures of heavy metal-transporting ATPases such as LpCopA and XtATP7B, both of which are in the E2-P$_i$ state (Figures S5E and S6).[37,38]

The ATP7B$_{apo}$ TMD consists of eight transmembrane helices (TMs), which are named MA, MB, and M1–6, following the nomenclature of those in LpCopA (Figure 2C).[37] Most TMs are straight helices in the transmembrane region, except MB, which bends by ~60° at two conserved glycines, Gly 710 and Gly711, which form the GG kink motif (Figure S6). The bent MB, together with MA, M1–2, M4, and M6, builds a cytosolic-facing cavity, which may allow the entry of the substrate copper from the cytosolic side (Figure 2D). By contrast, in structures of LpCopA and XtATP7B in the E2-P$_i$ state, this cavity is closed (Figure S5E). On the luminal side, the extracellular gate of ATP7B$_{apo}$ is closed by the packing of M1–2, M4, and M6 (Figure 2E). While MA, MB, M1, and M3–4 extend to the luminal surface of the membrane, the model suggests that the N-terminal ends of M2 and M6, as well as the C-terminal end of M5, sit deeply in the membrane at the luminal side, with a distance of ~20 Å between Cα atoms of the N-terminal residues in M6 and M4 (Figure 2E). This conformation of M2, M5, and M6 shortens the transmembrane distance and would likely favor the transport of the substrate copper across the membrane. Following the M6, a partial C-terminal tail (residues 1378–1405) that extends to the cytoplasm was resolved (Figures 2D and 2E). This portion of the C-terminal segment surrounds the P domain and may adjust the transport activity through the interaction with the P domain, as proposed in the structural analysis of XtATP7B.[38]

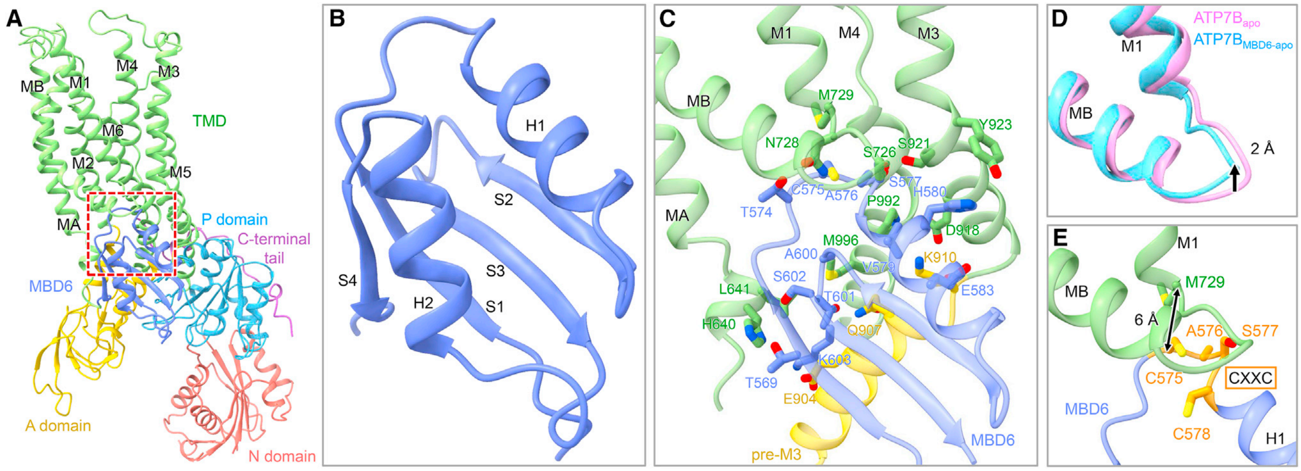

Figure 3. The MBD6 domain binds at the copper entry site

(A) Cartoon representation of ATP7B$_{MBD6\text{-}apo}$ in the same orientation as the map in Figure 2B. The red dashed box shows the copper entry site.

(B) Cartoon representation of MBD6.

(C) MBD6 interacts with the cytosolic copper entry site of the TMD. M2, M5, M6, and H2 in the MBD6 are omitted for clarity. Side chains involved in the interaction are shown as sticks.

(D) Superposition of ATP7B$_{apo}$ (pink) and ATP7B$_{MBD6\text{-}apo}$ (blue) when they are aligned at the entire transporter and zoomed-in view of the MB-M1 linker. The black arrow indicates an upward movement of the MB-M1 linker.

(E) Zoomed-in view of the copper entry site and CXXC motif in MBD6. Side chains of the CXXC motif (orange) and M729 (green) are shown as sticks. The black double arrow shows the distance between Cα atoms of C575 and M729.

The A domain in ATP7B$_{apo}$ is linked to M2 and M3 by two short helices, namely post-M2 and pre-M3, forming 120°–150° angles with M2 and M3, respectively (Figure 2D). The A domain is positioned at the opposite side of the P domain, without direct interaction with the N domain (Figure 2D). Compared with the A domain in other E1 state P-type ATPases such as the type II sarco/endoplasmic reticulum Ca^{2+}-ATPase (SERCA), the A domain in ATP7B$_{apo}$ moves backward from the N domain, leaving an ~18 Å gap between the A and N domains (Figures 2D and S5F). The P domain and N domain in ATP7B$_{apo}$ form close contact with each other and resemble those in the structure of SERCA in the E1 state (Figures 2D, 2E, and S5F).

To verify the functional relevance of the ATP7B$_{apo}$ structure, using the triple mutant of ATP7B, we further solved the ATP7B structure in complex with the ATP analog adenosine 5′-(β,γ-imido)triphosphate (AMP-PNP) at 4.0 Å resolution (ATP7B$_{AMP\text{-}PNP}$) (Figures S3K–S3O, S4I, and S4J). While this structure displays a very similar conformation as ATP7B$_{apo}$ in all the TMD, A, P, and N domains (Figure S5D), strong density between the P and N domains indicates that one AMP-PNP molecule is accommodated (Figure S4J), which induces an ~2 Å motion of the N domain closer to the P domain, a typical conformational change from the E1 to E1-ATP state in P-type ATPases (Figure S5D).[19] Thus, the ATP7B$_{AMP\text{-}PNP}$ structure likely represents an E1-ATP state structure of ATP7B. This ATP7B$_{AMP\text{-}PNP}$ structure supports that the high-resolution structures from the triple mutant can be used for the structure-function analysis of ATP7B.

The MBD6 domain binds at the copper entry site

In the structure of ATP7B$_{MBD6\text{-}apo}$, the MBD6 is assigned based on the local density at the cytoplasmic surface (Figures 2B and 3A), composed of two α helices (H1 and H2) and four antiparallel β strands (S1–S4) that form one β-sheet (Figure 3B). Three lines of evidence support that the density at the cytoplasmic surface is from the MBD6 instead of ATOX1, which shares a similar overall structure. First, the linker connecting the C-terminal end of the MBD6 and the N-terminal end of the MA helix was clearly resolved, as shown (Figure S4E). Second, the reported crystal structure of ATOX1 (PDB: 5T7L), with two residues missing in the S3-H2 linker, cannot fit well into the density of this putative MBD6 domain (Figure S4F). Third, the ATP7B$_{AMP\text{-}PNP}$ structure, which was determined using the sample of ATP7B without ATOX1, also maintains the density of the putative MBD6 (Figure S4I). ATOX1 may promote the proper orientation of the MBD6 toward the membrane copper entry site by interacting with the MBD2 or the MBD4 at the N-terminal of ATP7B, thus stabilizing the structure of the MBD6.[41–43] The absence of ATOX1 in the map can be due to its low ratio in the final sample and(or) its flexible binding with the MBDs (Figure S2G).

The MBD6 binds at the cytosolic entrance of the TMD and attaches to the MB and M1 helices by forming extensive interactions including hydrophobic packing and hydrogen bonds with MA, MB, M1, M3, M4, and the pre-M3 helix (Figures 3A and 3C). Compared with the ATP7B$_{apo}$ structure without the MBD6, the MB-M1 linker moves up by ~2 Å upon the binding of the MBD6 in the structure of ATP7B$_{MBD6\text{-}apo}$ (Figure 3D). The other parts of ATP7B$_{MBD6\text{-}apo}$ and ATP7B$_{apo}$ are basically the same, with a root-mean-square deviation (RMSD) of 1.001 Å over 728 Cα atoms when the two structures are aligned (Figure S5A).

In the MBD6, the CXXC motif located at the N-terminal end of the H1 helix involves in the coordination of heavy metal atoms such as Cu, Pt, Mo, and Cd, as revealed by structures of

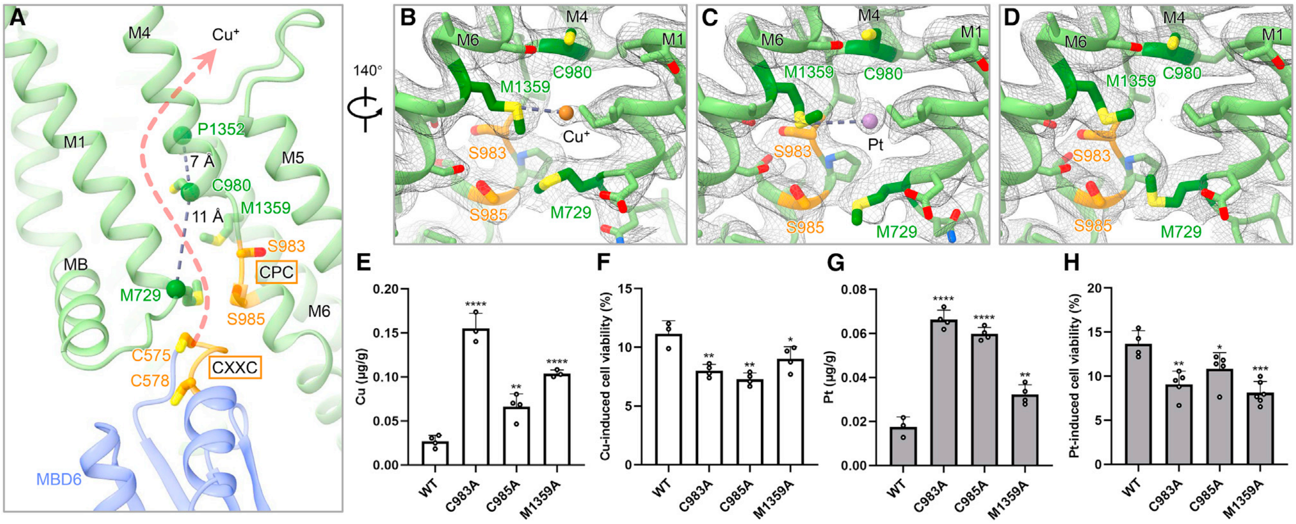

Figure 4. The potential copper and cisplatin transporting pathway

(A) The presumed copper and cisplatin transport pathway. MA, M2, and M3 are omitted for clarity. The CXXC and CPC (SPS) motifs are shown in orange. Critical residues lining the copper and cisplatin permeation path are shown as sticks. The two gray dashed lines show the distance between Cα atoms of M729 and C980, and Cα atoms of C980 and P1352, respectively. The red dashed arrow indicates the presumed copper and cisplatin transport pathway.

(B) Representation of the densities of copper and side chains of key residues for substrate coordination in ATP7B$_{\text{MBD6-Cu}}$ at the contour level of 4.5 σ, sharpened with a B factor of −140.0. The dashed line indicates the main coordination of copper by M1359.

(C) Representation of the densities of cisplatin and side chains of key residues for substrate coordination in ATP7B$_{\text{MBD6-Pt}}$ at the contour level of 4.5 σ, sharpened with a B factor of −215.5. The dashed line indicates the main coordination of cisplatin by M1359.

(D) Representation of the densities of side chains of key residues for substrate coordination in ATP7B$_{\text{MBD6-apo}}$ at the contour level of 4.5 σ, sharpened with a B factor of −40.0. No density is observed in the putative metal-binding site in the map.

(E and F) The effect of ATP7B mutants (C983A, C985A, and M1359A) on HEK293T cellular metal accumulation and cell viability following exposure to copper. Data are expressed as mean ± SD ($n \geq 3$, *$p < 0.05$, **$p < 0.01$, ****$p < 0.0001$).

(G and H) The effect of ATP7B mutants (C983A, C985A, and M1359A) on HEK293T cellular metal accumulation and cell viability following exposure to cisplatin. Data are expressed as mean ± SD ($n \geq 3$, *$p < 0.05$, **$p < 0.01$, ***$p < 0.001$, ****$p < 0.0001$).

MBDs in ATP7B and its homologous domain MNKs in ATP7A.[44–46] In the structure of ATP7B$_{\text{MBD6-apo}}$, the CXXC motif in the MBD6 is positioned adjacent to the copper entry site. Cys575 sits just below the Met729 in the N-terminal end of M1, with a distance of ~6 Å between Cα atoms of the two residues (Figure 3E). This pose of the MBD6 would allow the copper bound at the CXXC motif to be delivered to the CPC motif in M4 via the Met729 in M1. The essential role of the CXXC motif of the MBD6 in copper transport has been verified by previous studies.[24–26] Taken together, this ATP7B$_{\text{MBD6-apo}}$ structure here clearly shows how the MBD6 is recognized by TMD.

The potential copper and cisplatin transporting pathway

The structure of ATP7B$_{\text{MBD6-apo}}$ deciphers the potential copper transport pathway from MBD6 across the TMD to the luminal side, similar to previous analyses for LpCopA and XtATP7B.[37,38] Different from other stable metal ions, copper is transported as Cu^+, which has redox activity and is usually coordinated by sulfur-containing residues such as Met and Cys.[47] The potential copper transport pathway in the TMD of ATP7B is marked by these sulfur-containing residues, including Cys578 and Cys575 (the CXXC motif) in the MBD6, Met729 in M1, Cys985 and Cys983 (the CPC motif) in M4, Met1359 in M6, and Cys980 in M4 (Figure 4A). Except Cys980, all those residues are conserved among the three copper-transporting ATPases (Figure S6). Cu^+ is likely to be passed from the CXXC motif in the MBD6 via Met729, CPC motif, Met1359, and finally to Cys980 across 11–12 Å (Figure 4A). The 5–7 Å short distance between Cys980 and the conserved residue Pro1352 in the N-terminal end of M6 makes Cu^+ be released to the luminal side readily (Figure 4A).

To validate this copper transport pathway, we determined the structures of the ATP7B-ATOX1 complex in the presence of copper (ATP7B$_{\text{MBD6-Cu}}$) or cisplatin (ATP7B$_{\text{MBD6-Pt}}$). In the 3.6 Å resolution map of ATP7B$_{\text{MBD6-Cu}}$, weak but decent density surrounded by Met729, Met1359, and Cys980 is observed (Figure 4B). A similar but stronger density is also observed in the same site in the map of ATP7B$_{\text{MBD6-Pt}}$ (Figure 4C). As a control, no similar density is found in the same site in the map of ATP7B$_{\text{MBD6-apo}}$ (Figure 4D). Therefore, we tentatively modeled Cu^+ and Pt in this site in the structures of ATP7B$_{\text{MBD6-Cu}}$ and ATP7B$_{\text{MBD6-Pt}}$, respectively. Both putative Cu^+ and Pt are mainly coordinated by Met1359 (Figures 4B and 4C). As the two Cys residues in the CPC motif were mutated to Ser residues, no density of Cu^+ or Pt is observed in the vicinity of these two residues (Figures S4G and S4H). Nevertheless, as Cu^+ ions need to be passed from the MBD6 to the luminal side, there should be multiple Cu^+ binding sites along the transport pathway.[48]

To further confirm the essential role of these sulfur-containing residues in the copper transport process, we measured the copper transport activity of ATP7B with mutations at these potential

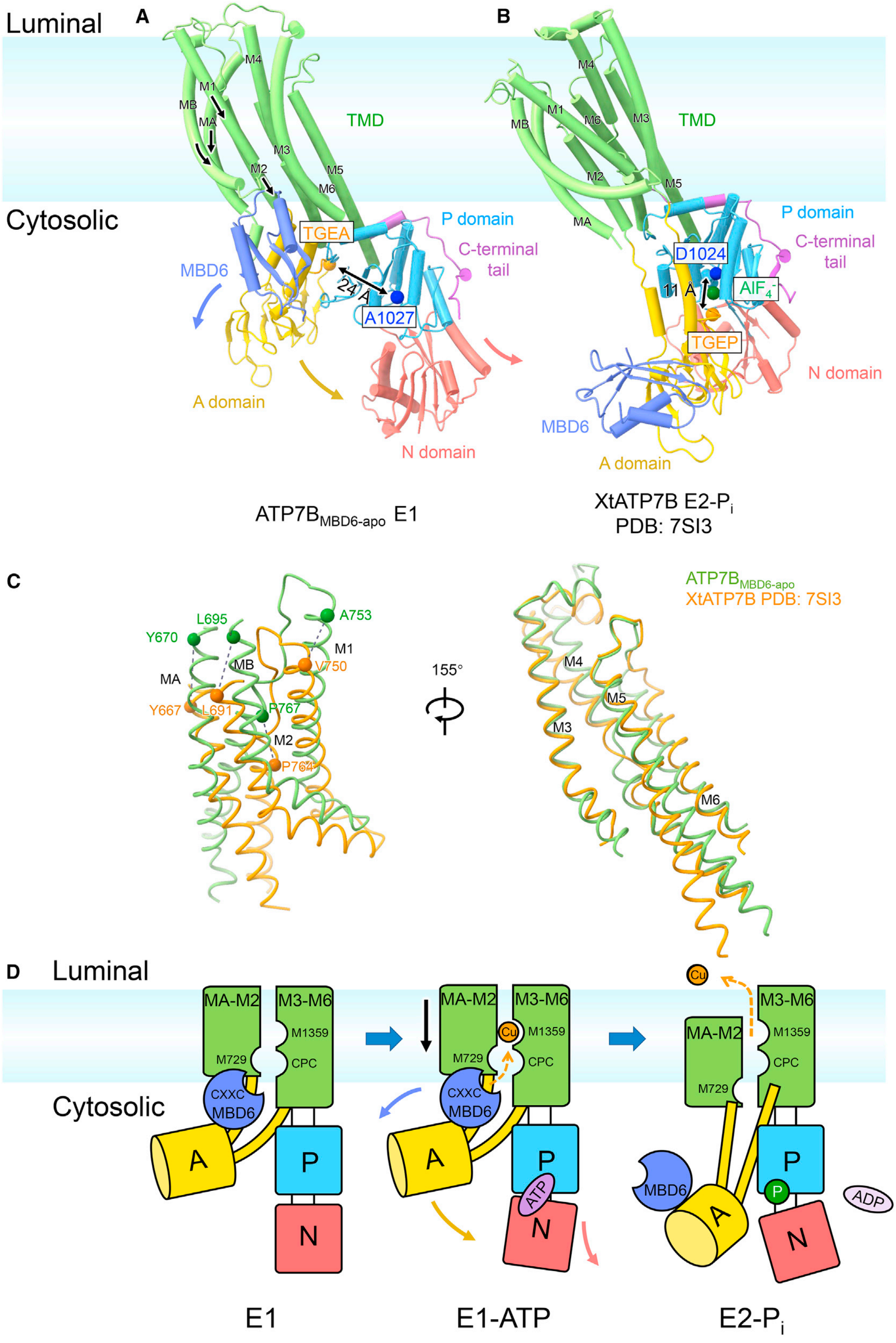

(legend on next page)

copper-interaction residues, namely Cys983, Cys985, and Met1359. Compared with the WT, all three mutants, C983A, C985A, and M1359A, displayed similar expression levels (Figure S1) but impaired copper transport activity, as indicated by the increased copper accumulation in cells expressing these ATP7B mutants under the treatment of copper (Figure 4E). Consistently, the viability of the cells expressing these ATP7B mutants was lower than those expressing WT ATP7B (Figure 4F). Similarly, cells expressing these mutants also displayed increased Pt accumulation and lower cell viability than those expressing WT ATP7B under the treatment of cisplatin (Figures 4G and 4H). Therefore, these transport activity results confirm the important role of the three sulfur-containing residues in the copper and cisplatin transport process. We also evaluated the transport activity of ATP7B with mutations at other residues along the transport pathway, namely Cys575, Cys578, Met729, and Cys980. We found that compared with WT ATP7B, all four mutants, C575A, C578A, M729A, and C980A, impaired the copper transport activity of ATP7B rather than the cisplatin transport activity, as revealed by the metal accumulation and cell viability experiments (Figure S1). This may imply that the mode of cisplatin transported by ATP7B differs to some extent from that of copper.

Conformational change of ATP7B in the transport cycle

Since our structures are in the E1 state, comparisons of our structures with previous structures of LpCopA and XtATP7B in the E2-P_i state can help elucidate the transport mechanisms of ATP7B. Here, we compared the ATP7B$_{\text{MBD6-apo}}$ structure in the E1 state and the XtATP7B in the E2-P_i state, revealing conformational changes of multiple domains in the transport cycle (Figures 5A and 5B). First, in ATP7B$_{\text{MBD6-apo}}$, the A domain is detached from the N domain, with an ~24 Å distance between Glu860 in the TGEA motif in the A domain and the phosphorylation site Asp1027 (Ala1027) in the P domain. In comparison, in XtATP7B, the A domain interacts with both N and P domains. The distance between Glu857 and Asp1024 becomes ~11 Å. The Glu in the TGEP motif of the A domain coordinates a water molecule, which performs a nucleophilic attack on the phosphate bond of phosphorylated Asp in the P domain and triggers the dephosphorylation.[19] Second, without the A domain nearby, the N domain in ATP7B$_{\text{MBD6-apo}}$ is closer to the P domain compared with that in XtATP7B. Third, the MBD6, which is attached to the TMD at the copper entry site in ATP7B$_{\text{MBD6-apo}}$, dissociates from the TMD and relocates to the A domain in XtATP7B. Fourth, different from the closed luminal/extracellular gate in ATP7B$_{\text{MBD6-apo}}$, the luminal gate in XtATP7B opens up due to the motion of MA–B and M1–2 down to the cytosolic side by ~3 helical turns (Figure 5C).

According to the structures of ATP7B$_{\text{MBD6-apo}}$, ATP7B$_{\text{AMP-PNP}}$, and XtATP7B, as well as the accumulated structure data of other P-type ATPases such as SERCA and Na^+/K^+-ATPase, we propose an ATP7B-mediated copper transport model. The MBD6 passes the Cu^+ from its CXXC motif to the CPC motif in M4. The Cu^+ will be further passed up to a second site close to the conserved Met1359, as indicated by the putative substrate density in the structures of ATP7B$_{\text{MBD6-Cu}}$ and ATP7B$_{\text{MBD6-Pt}}$. Along with the binding of ATP between the N and P domains, the phosphorylation of Asp1027, and the release of ADP from the N domain, ATP7B occupies a series of intermediate states from E1 via E1-ATP, E1P-ADP, E2P-ADP, and E2P and finally to E2-P_i.[19] The A domain then rotates and moves close to the nucleotide-binding pocket between the N and P domains, along with the detachment of the MBD6 from the TMD. The A domain is linked to M2 and M3 by two helices named post-M2 and pre-M3 in the E1 state. After rotation, the two helices are almost in line with M2 and M3. This large conformational change of the A domain further induces structural rearrangement of MA–B and M1–2 in the TMD, which are pulled down to the cytosolic side by ~3 helical turns, allowing the closing of the cytosolic gate and the opening of the luminal/extracellular gate. Then, the Cu^+ will be released to the luminal/extracellular side (Figure 5D; Videos S1 and S2).

Analysis of WD pathogenic variants

Our cryo-EM structure model of human ATP7B serves as a framework for studying WD mutations. Of all identified WD pathogenic mutations, missense mutations account for more than half.[15,16] We mapped some of them onto our cryo-EM structure of ATP7B$_{\text{MBD6-apo}}$. As shown in Figure 6A, the mutations are distributed throughout the TMD and cytosolic domains of ATP7B, indicating the indispensability of each domain. Most of the mutations are located in the structurally resolved regions of the enzyme that are important for the transport function coupled with ATP binding and hydrolysis, including those frequent mutations such as p.R778L in East Asian countries[15,49] and p.H1069Q in Europe[50] (Figure 6). In the structure, His1069 is located in the N domain and is directly involved in the ATP binding by forming hydrogen bonds with the α phosphate group (Figure 6C). Mutation on His1069 likely affects the ATP binding and the copper transport activity. Arg778 in M2 sits in the vicinity of cytoplasmic copper entry site Met729 and forms a salt bridge with Asp730 in M1 (Figure 6B), which may stabilize the

Figure 5. Conformational change of ATP7B in the transport cycle

(A) Side view of ATP7B$_{\text{MBD6-apo}}$ in the E1 state. The Cα atoms of E860 in the TGEA motif and A1027 are shown as orange and blue spheres, respectively. The black double arrow shows the distance between E860 and A1027. The black arrows indicate the downward movement of MA, MB, M1, and M2. The purple-blue arrow, yellow arrow, and red arrow indicate the movement of the MBD6, A domain, and N domain, respectively.

(B) Side view of XtATP7B in the E2-P_i state. The MBD5 is omitted for clarity. The Cα atoms of E857 in the TGEP motif, D1024, and Al ion are shown as orange, blue, and green spheres, respectively. The black double arrow shows the distance between E857 and D1024.

(C) Side view of the superposition of the TMD in ATP7B$_{\text{MBD6-apo}}$ (green) and XtATP7B (orange) when they are aligned at M3–M6. M3–M6 are omitted for clarity (left). MA-B and M1-2 are omitted for clarity (right). The spheres indicate the Cα atoms of equivalent residues in the N-terminal ends of MA-B and M1-2.

(D) Proposed mechanism of copper transport. Schematic model of copper transport mediated by ATP7B. The model is depicted with the same color codes as in Figure 2C. Cu^+ is shown as an orange circle and an orange dashed arrow indicates the Cu^+ transport pathway. The black arrow, purple-blue arrow, yellow arrow, and red arrow indicate the movement of the TMD, MBD6, A domain, and N domain, respectively.

Also, see Videos S1 and S2.

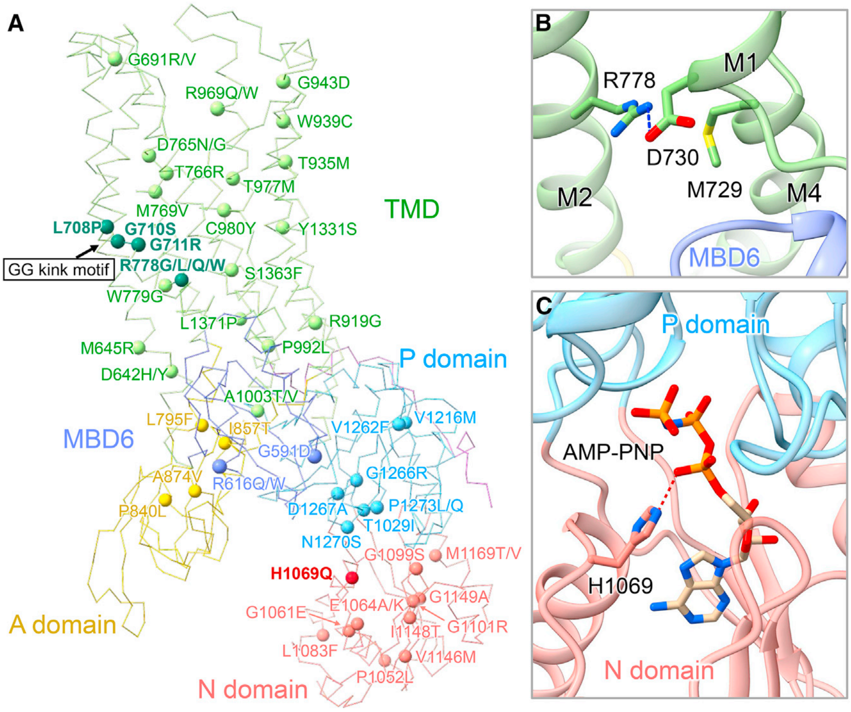

Figure 6. Wilson disease mutations

(A) The Wilson disease mutations are mapped onto the ATP7B$_{\text{MBD6-apo}}$ structure. The frequent mutations p.R778L and p.H1069Q and mutations in the GG kink motif are highlighted.

(B) The zoomed-in structure of R778. The blue dashed line indicates that R778 forms a salt bridge with D730.

(C) The zoomed-in structure of H1069. The red dashed line indicates that H1069 forms hydrogen bonds with the α phosphate group of AMP-PNP.

conformation of the TMD in the E1 state. The mutation p.R778L would destroy this salt bridge along with diminished transport activity and serious phenotype.[51,52] In addition, another mutation p.C980Y also lies in the transporting pathway and may attenuate the copper transport. Interestingly, the GG kink motif of MB acts as a specific region for clinical mutations including p.G710S, p.G711R, and p.L708P (Figure 6A). It is also worth mentioning that most of mutations in the N-terminal MBDs are located at the MBD6 (p.G591D and p.R616Q/W), indicating the significant role of the MBD6 for the transport activity.

DISCUSSION

The ATP7B$_{\text{MBD6-apo}}$ structure reveals how the MBD6 delivers copper to the cytosolic entry site in the TMD. In addition, we observed weak density between the MBD6 and the A domain, with the shape analogous to the MBD6 (Figure S7A). Considering that the MBD5 and the MBD6 form a compact unit, while MBD1–MBD4 are flexibly connected,[29,53] we speculate that the density may be from the MBD5. As both the MBD5 and the MBD6 form strong interactions with the A domain in the XtATP7B structure, to reveal the possible movement of the MBD5 and the MBD6 from the E1 to E2-P$_i$ state, we aligned the structures of ATP7B$_{\text{MBD6-apo}}$ and XtATP7B at the A domain (Figure S7B). Interestingly, the putative MBD5 in ATP7B$_{\text{MBD6-apo}}$ almost occupies the MBD6 site in XtATP7B, which suggests a possible consecutive movement of the MBD5 and the MBD6 from the E1 to E2-P$_i$ state. From the E1 to E2-P$_i$ state, along with the relocation of the A domain, the MBD5 likely rotates by $\sim$90° and moves from the top side of the A domain to the right, making space for the MBD6, which releases from the TMD and attaches to the A domain (Figure S7C). As the MBD6 and the MBD5 form weak interactions in XtATP7B, we also overlay the XtATP7B on ATP7B$_{\text{MBD6-apo}}$ by aligning the MBD6 (Figure S7D), which shows that the MBD5 from XtATP7B is located underneath the MBD6 in ATP7B$_{\text{MBD6-apo}}$ and cannot fit into the putative MBD5 density. Thus, the relative position of the MBD5 and the MBD6 is likely rearranged from the E1 to E2-P$_i$ state.

In the structure of ATOX1 dimer, copper is coordinated by four cysteines, two from each subunit.[54] Based on this, the formation of an ATOX1-MBD hetero-dimer was speculated to be the mechanism for copper passage from ATOX1 to the MBD. In the ATP7B$_{\text{MBD6-Cu}}$ structure, the MBD6 attaches to the TMD with the copper coordination CXXC motif toward the copper entry site (Figure 4A). Thus, the potential ATOX1 interaction surface is buried, preventing the formation of an ATOX1-MBD6 dimer. This conformation of the MBD6 represents a copper delivering state instead of an accepting state. By contrast, the copper-binding site in the MBD6 in the XtATP7B structure is exposed and may accept copper from ATOX1 (Figure S5G).[38] In addition, no copper density was observed in the CXXC motif of the MBD6 in the map of ATP7B$_{\text{MBD6-Cu}}$. One possible reason is that the CXXC motif in the MBD6 displays a relatively low copper-binding affinity compared with the copper-binding sites in the TMD when copper is translocated.[24] Moreover, the low local map quality hinders the observation of potential copper in the CXXC motif of the MBD6 (Figure S4G).

Conclusions

In this study, we determined the cryo-EM structures of human ATP7B in the E1 state. These structures show how the MBD6 binds and delivers cytosolic copper to the TMD. By analyzing the sulfur-containing residues in the TMD, we decipher the copper and cisplatin transport pathway and validate it by metal transport assay. Furthermore, by comparing structures of the E1 state human ATP7B and E2-P$_i$ state XtATP7B, we propose the ATP-driving copper transport model of ATP7B. Considering the important role of ATP7B in the regulation of cellular copper homeostasis and cisplatin resistance, the structures of ATP7B will advance our understanding of the molecular mechanisms of copper and cisplatin export and guide the treatment of ATP7B-related WD and cisplatin resistance.

Limitations of the study

To increase the protein expression level for the structural study, we introduced three single mutations at the active sites in ATP7B, which prevented us from exploring other states of ATP7B in the transport cycle to better elucidate the translocation mechanisms. In addition, although we have resolved the MBD6 in the current structures, other MBDs and the intact C-terminal tail as well as ATOX1 were unresolved, and their roles in the transport activity remain to be investigated. Moreover, the resolution of the copper- or cisplatin-bound structure needs to be further improved to strengthen related interpretations.

STAR★METHODS

Detailed methods are provided in the online version of this paper and include the following:

- KEY RESOURCES TABLE
- RESOURCE AVAILABILITY
  - ○ Lead contact
  - ○ Materials availability
  - ○ Data and code availability
- EXPERIMENTAL MODEL AND SUBJECT DETAILS
  - ○ Insect cell lines
  - ○ Human cell lines
- METHOD DETAILS
  - ○ Protein expression and purification
  - ○ Cryo-EM sample preparation and data acquisition
  - ○ Image processing
  - ○ Model building, refinement, and validation
  - ○ Mutagenesis, cell culture, and transient transfection
  - ○ Western blotting
  - ○ Cell viability assay
  - ○ Intracellular copper and cisplatin accumulation
- QUANTIFICATION AND STATISTICAL ANALYSIS

SUPPLEMENTAL INFORMATION

Supplemental information can be found online at https://doi.org/10.1016/j.celrep.2023.112417.

ACKNOWLEDGMENTS

Single-particle cryo-EM data were collected at the Centers of Cryo-Electron Microscopy at Zhejiang University and Hubei University. We thank Dr. Xing Zhang for support in facility access and data acquisition. This work was supported in part by the National Natural Science Foundation of China (81125009 to Z.-Y.W.) and the Ministry of Science and Technology (2020YFA0908501 to J.G. and 2020YFA0908400 to S.W.).

AUTHOR CONTRIBUTIONS

Z.-Y.W., J.G., and S.W. conceived and supervised the project. G.-M.Y., L.X., D.M., and C.Z. prepared the samples. G.-M.Y., L.X., X.T., and S.C. performed data acquisition, structure determination, and data analysis. G.-M.Y., R.-M.W., and Z.-W.Z. performed the metal transport assay. All authors participated in the data analysis and paper preparation.

DECLARATION OF INTERESTS

The authors declare no competing interests.

Received: October 20, 2022
Revised: February 22, 2023
Accepted: April 5, 2023
Published: April 18, 2023

REFERENCES

1. Harris, E.D. (2000). Cellular copper transport and metabolism. Annu. Rev. Nutr. *20*, 291–310. https://doi.org/10.1146/annurev.nutr.20.1.291.
2. Lutsenko, S. (2010). Human copper homeostasis: a network of interconnected pathways. Curr. Opin. Chem. Biol. *14*, 211–217. https://doi.org/10.1016/j.cbpa.2010.01.003.
3. Linz, R., and Lutsenko, S. (2007). Copper-transporting ATPases ATP7A and ATP7B: cousins, not twins. J. Bioenerg. Biomembr. *39*, 403–407. https://doi.org/10.1007/s10863-007-9101-2.
4. Inesi, G., Pilankatta, R., and Tadini-Buoninsegni, F. (2014). Biochemical characterization of P-type copper ATPases. Biochem. J. *463*, 167–176. https://doi.org/10.1042/bj20140741.
5. Scheiber, I.F., Brůha, R., and Dušek, P. (2017). Pathogenesis of Wilson disease. Handb. Clin. Neurol. *142*, 43–55. https://doi.org/10.1016/b978-0-444-63625-6.00005-7.
6. Członkowska, A., Litwin, T., Dusek, P., Ferenci, P., Lutsenko, S., Medici, V., Rybakowski, J.K., Weiss, K.H., and Schilsky, M.L. (2018). Wilson disease. Nat. Rev. Dis. Primers *4*, 21. https://doi.org/10.1038/s41572-018-0018-3.
7. European Association for Study of Liver (2012). EASL clinical practice guidelines: Wilson's disease. J. Hepatol. *56*, 671–685. https://doi.org/10.1016/j.jhep.2011.11.007.
8. Peng, F. (2014). Positron emission tomography for measurement of copper fluxes in live organisms. Ann. N. Y. Acad. Sci. *1314*, 24–31. https://doi.org/10.1111/nyas.12383.
9. Merle, U., Schaefer, M., Ferenci, P., and Stremmel, W. (2007). Clinical presentation, diagnosis and long-term outcome of Wilson's disease: a cohort study. Gut *56*, 115–120. https://doi.org/10.1136/gut.2005.087262.
10. Dong, Y., Wang, R.M., Yang, G.M., Yu, H., Xu, W.Q., Xie, J.J., Zhang, Y., Chen, Y.C., Ni, W., and Wu, Z.Y. (2021). Role for biochemical assays and Kayser-Fleischer rings in diagnosis of Wilson's disease. Clin. Gastroenterol. Hepatol. *19*, 590–596. https://doi.org/10.1016/j.cgh.2020.05.044.
11. Roberts, E.A., and Schilsky, M.L.; American Association for Study of Liver Diseases AASLD (2008). Diagnosis and treatment of Wilson disease: an update. Hepatology *47*, 2089–2111. https://doi.org/10.1002/hep.22261.
12. Dong, Q.Y., and Wu, Z.Y. (2012). Advance in the pathogenesis and treatment of Wilson disease. Transl. Neurodegener. *1*, 23. https://doi.org/10.1186/2047-9158-1-23.
13. Ahmad, A., Torrazza-Perez, E., and Schilsky, M.L. (2017). Liver transplantation for Wilson disease. Handb. Clin. Neurol. *142*, 193–204. https://doi.org/10.1016/b978-0-444-63625-6.00016-1.
14. Huster, D., Kühne, A., Bhattacharjee, A., Raines, L., Jantsch, V., Noe, J., Schirrmeister, W., Sommerer, I., Sabri, O., Berr, F., et al. (2012). Diverse functional properties of Wilson disease ATP7B variants. Gastroenterology *142*, 947–956.e5. https://doi.org/10.1053/j.gastro.2011.12.048.
15. Dong, Y., Ni, W., Chen, W.J., Wan, B., Zhao, G.X., Shi, Z.Q., Zhang, Y., Wang, N., Yu, L., Xu, J.F., et al. (2016). Spectrum and classification of ATP7B variants in a large cohort of Chinese patients with Wilson's disease guides genetic diagnosis. Theranostics *6*, 638–649. https://doi.org/10.7150/thno.14596.
16. Chang, I.J., and Hahn, S.H. (2017). The genetics of Wilson disease. Handb. Clin. Neurol. *142*, 19–34. https://doi.org/10.1016/b978-0-444-63625-6.00003-3.
17. Argüello, J.M., Eren, E., and González-Guerrero, M. (2007). The structure and function of heavy metal transport P1B-ATPases. Biometals *20*, 233–248. https://doi.org/10.1007/s10534-006-9055-6.

18. Kühlbrandt, W. (2004). Biology, structure and mechanism of P-type ATPases. Nat. Rev. Mol. Cell Biol. *5*, 282–295. https://doi.org/10.1038/nrm1354.

19. Dyla, M., Kjærgaard, M., Poulsen, H., and Nissen, P. (2020). Structure and mechanism of P-type ATPase ion pumps. Annu. Rev. Biochem. *89*, 583–603. https://doi.org/10.1146/annurev-biochem-010611-112801.

20. Albers, R.W. (1967). Biochemical aspects of active transport. Annu. Rev. Biochem. *36*, 727–756. https://doi.org/10.1146/annurev.bi.36.070167.003455.

21. Post, R.L., Kume, S., Tobin, T., Orcutt, B., and Sen, A.K. (1969). Flexibility of an active center in sodium-plus-potassium adenosine triphosphatase. J. Gen. Physiol. *54*, 306–326. https://doi.org/10.1085/jgp.54.1.306.

22. Argüello, J.M. (2003). Identification of ion-selectivity determinants in heavy-metal transport P1B-type ATPases. J. Membr. Biol. *195*, 93–108. https://doi.org/10.1007/s00232-003-2048-2.

23. Ariöz, C., Li, Y., and Wittung-Stafshede, P. (2017). The six metal binding domains in human copper transporter, ATP7B: molecular biophysics and disease-causing mutations. Biometals *30*, 823–840. https://doi.org/10.1007/s10534-017-0058-2.

24. Huster, D., and Lutsenko, S. (2003). The distinct roles of the N-terminal copper-binding sites in regulation of catalytic activity of the Wilson's disease protein. J. Biol. Chem. *278*, 32212–32218. https://doi.org/10.1074/jbc.M305408200.

25. Cater, M.A., Forbes, J., La Fontaine, S., Cox, D., and Mercer, J.F.B. (2004). Intracellular trafficking of the human Wilson protein: the role of the six N-terminal metal-binding sites. Biochem. J. *380*, 805–813. https://doi.org/10.1042/bj20031804.

26. Guo, Y., Nyasae, L., Braiterman, L.T., and Hubbard, A.L. (2005). NH2-terminal signals in ATP7B Cu-ATPase mediate its Cu-dependent anterograde traffic in polarized hepatic cells. Am. J. Physiol. Gastrointest. Liver Physiol. *289*, G904–G916. https://doi.org/10.1152/ajpgi.00262.2005.

27. Walker, J.M., Tsivkovskii, R., and Lutsenko, S. (2002). Metallochaperone Atox1 transfers copper to the NH2-terminal domain of the Wilson's disease protein and regulates its catalytic activity. J. Biol. Chem. *277*, 27953–27959. https://doi.org/10.1074/jbc.M203845200.

28. Yatsunyk, L.A., and Rosenzweig, A.C. (2007). Cu(I) binding and transfer by the N terminus of the Wilson disease protein. J. Biol. Chem. *282*, 8622–8631. https://doi.org/10.1074/jbc.M609533200.

29. Banci, L., Bertini, I., Cantini, F., Massagni, C., Migliardi, M., and Rosato, A. (2009). An NMR study of the interaction of the N-terminal cytoplasmic tail of the Wilson disease protein with copper(I)-HAH1. J. Biol. Chem. *284*, 9354–9360. https://doi.org/10.1074/jbc.M805981200.

30. Furukawa, T., Komatsu, M., Ikeda, R., Tsujikawa, K., and Akiyama, S.i. (2008). Copper transport systems are involved in multidrug resistance and drug transport. Curr. Med. Chem. *15*, 3268–3278. https://doi.org/10.2174/092986708786848479.

31. Arnesano, F., and Natile, G. (2021). Interference between copper transport systems and platinum drugs. Semin. Cancer Biol. *76*, 173–188. https://doi.org/10.1016/j.semcancer.2021.05.023.

32. Dolgova, N.V., Olson, D., Lutsenko, S., and Dmitriev, O.Y. (2009). The soluble metal-binding domain of the copper transporter ATP7B binds and detoxifies cisplatin. Biochem. J. *419*, 51–56. https://doi.org/10.1042/bj20081359.

33. Safaei, R., Adams, P.L., Maktabi, M.H., Mathews, R.A., and Howell, S.B. (2012). The CXXC motifs in the metal binding domains are required for ATP7B to mediate resistance to cisplatin. J. Inorg. Biochem. *110*, 8–17. https://doi.org/10.1016/j.jinorgbio.2012.02.016.

34. Katano, K., Safaei, R., Samimi, G., Holzer, A., Tomioka, M., Goodman, M., and Howell, S.B. (2004). Confocal microscopic analysis of the interaction between cisplatin and the copper transporter ATP7B in human ovarian carcinoma cells. Clin. Cancer Res. *10*, 4578–4588. https://doi.org/10.1158/1078-0432.ccr-03-0689.

35. Tadini-Buoninsegni, F., Bartolommei, G., Moncelli, M.R., Inesi, G., Galliani, A., Sinisi, M., Losacco, M., Natile, G., and Arnesano, F. (2014). Translocation of platinum anticancer drugs by human copper ATPases ATP7A and ATP7B. Angew. Chem. Int. Ed. Engl. *53*, 1297–1301. https://doi.org/10.1002/anie.201307718.

36. Mariniello, M., Petruzzelli, R., Wanderlingh, L.G., La Montagna, R., Carissimo, A., Pane, F., Amoresano, A., Ilyechova, E.Y., Galagudza, M.M., Catalano, F., et al. (2020). Synthetic lethality screening identifies FDA-approved drugs that overcome ATP7B-mediated tolerance of tumor cells to cisplatin. Cancers *12*, 608. https://doi.org/10.3390/cancers12030608.

37. Gourdon, P., Liu, X.Y., Skjørringe, T., Morth, J.P., Møller, L.B., Pedersen, B.P., and Nissen, P. (2011). Crystal structure of a copper-transporting PIB-type ATPase. Nature *475*, 59–64. https://doi.org/10.1038/nature10191.

38. Bitter, R.M., Oh, S., Deng, Z., Rahman, S., Hite, R.K., and Yuan, P. (2022). Structure of the Wilson disease copper transporter ATP7B. Sci. Adv. *8*, eabl5508. https://doi.org/10.1126/sciadv.abl5508.

39. Valko, M., Morris, H., and Cronin, M.T.D. (2005). Metals, toxicity and oxidative stress. Curr. Med. Chem. *12*, 1161–1208. https://doi.org/10.2174/0929867053764635.

40. Barabas, K., Milner, R., Lurie, D., and Adin, C. (2008). Cisplatin: a review of toxicities and therapeutic applications. Vet. Comp. Oncol. *6*, 1–18. https://doi.org/10.1111/j.1476-5829.2007.00142.x.

41. Lutsenko, S., Barnes, N.L., Bartee, M.Y., and Dmitriev, O.Y. (2007). Function and regulation of human copper-transporting ATPases. Physiol. Rev. *87*, 1011–1046. https://doi.org/10.1152/physrev.00004.2006.

42. Yu, C.H., Yang, N., Bothe, J., Tonelli, M., Nokhrin, S., Dolgova, N.V., Braiterman, L., Lutsenko, S., and Dmitriev, O.Y. (2017). The metal chaperone Atox1 regulates the activity of the human copper transporter ATP7B by modulating domain dynamics. J. Biol. Chem. *292*, 18169–18177. https://doi.org/10.1074/jbc.M117.811752.

43. Shanmugavel, K.P., and Wittung-Stafshede, P. (2019). Copper relay path through the N-terminus of Wilson disease protein. Metallomics *11*, 1472–1480. https://doi.org/10.1039/c9mt00147f.

44. Banci, L., Bertini, I., Calderone, V., Della-Malva, N., Felli, I.C., Neri, S., Pavelkova, A., and Rosato, A. (2009). Copper(I)-mediated protein-protein interactions result from suboptimal interaction surfaces. Biochem. J. *422*, 37–42. https://doi.org/10.1042/bj20090422.

45. Fang, T., Chen, W., Sheng, Y., Yuan, S., Tang, Q., Li, G., Huang, G., Su, J., Zhang, X., Zang, J., et al. (2019). Tetrathiomolybdate induces dimerization of the metal-binding domain of ATPase and inhibits platination of the protein. Nat. Commun. *10*, 186. https://doi.org/10.1038/s41467-018-08102-z.

46. Lasorsa, A., Nardella, M.I., Rosato, A., Mirabelli, V., Caliandro, R., Caliandro, R., Natile, G., and Arnesano, F. (2019). Mechanistic and structural basis for inhibition of copper trafficking by platinum anticancer drugs. J. Am. Chem. Soc. *141*, 12109–12120. https://doi.org/10.1021/jacs.9b05550.

47. Mattle, D., Zhang, L., Sitsel, O., Pedersen, L.T., Moncelli, M.R., Tadini-Buoninsegni, F., Gourdon, P., Rees, D.C., Nissen, P., and Meloni, G. (2015). A sulfur-based transport pathway in Cu+-ATPases. EMBO Rep. *16*, 728–740. https://doi.org/10.15252/embr.201439927.

48. Andersson, M., Mattle, D., Sitsel, O., Klymchuk, T., Nielsen, A.M., Møller, L.B., White, S.H., Nissen, P., and Gourdon, P. (2014). Copper-transporting P-type ATPases use a unique ion-release pathway. Nat. Struct. Mol. Biol. *21*, 43–48. https://doi.org/10.1038/nsmb.2721.

49. Yang, G.M., Wang, R.M., Xia, N., Zheng, Z.W., Dong, Y., and Wu, Z.Y. (2021). Prevalent pathogenic variants of ATP7B in Chinese patients with Wilson's disease: geographical distribution and founder effect. Genes *12*, 336. https://doi.org/10.3390/genes12030336.

50. Ferenci, P. (2006). Regional distribution of mutations of the ATP7B gene in patients with Wilson disease: impact on genetic testing. Hum. Genet. *120*, 151–159. https://doi.org/10.1007/s00439-006-0202-5.

51. Wu, Z.Y., Wang, N., Lin, M.T., Fang, L., Murong, S.X., and Yu, L. (2001). Mutation analysis and the correlation between genotype and phenotype

of Arg778Leu mutation in Chinese patients with Wilson disease. Arch. Neurol. *58*, 971–976. https://doi.org/10.1001/archneur.58.6.971.

52. Zhu, M., Dong, Y., Ni, W., and Wu, Z.Y. (2015). Defective roles of ATP7B missense mutations in cellular copper tolerance and copper excretion. Mol. Cell. Neurosci. *67*, 31–36. https://doi.org/10.1016/j.mcn.2015.05.005.
53. Achila, D., Banci, L., Bertini, I., Bunce, J., Ciofi-Baffoni, S., and Huffman, D.L. (2006). Structure of human Wilson protein domains 5 and 6 and their interplay with domain 4 and the copper chaperone HAH1 in copper uptake. Proc. Natl. Acad. Sci. USA *103*, 5729–5734. https://doi.org/10.1073/pnas.0504472103.
54. Wernimont, A.K., Huffman, D.L., Lamb, A.L., O'Halloran, T.V., and Rosenzweig, A.C. (2000). Structural basis for copper transfer by the metallochaperone for the Menkes/Wilson disease proteins. Nat. Struct. Biol. *7*, 766–771. https://doi.org/10.1038/78999.
55. Scheres, S.H.W. (2012). RELION: implementation of a Bayesian approach to cryo-EM structure determination. J. Struct. Biol. *180*, 519–530. https://doi.org/10.1016/j.jsb.2012.09.006.
56. Punjani, A., Rubinstein, J.L., Fleet, D.J., and Brubaker, M.A. (2017). cryoSPARC: algorithms for rapid unsupervised cryo-EM structure determination. Nat. Methods *14*, 290–296. https://doi.org/10.1038/nmeth.4169.
57. Emsley, P., Lohkamp, B., Scott, W.G., and Cowtan, K. (2010). Features and development of Coot. Acta Crystallogr. D Biol. Crystallogr. *66*, 486–501. https://doi.org/10.1107/s0907444910007493.
58. Adams, P.D., Afonine, P.V., Bunkóczi, G., Chen, V.B., Davis, I.W., Echols, N., Headd, J.J., Hung, L.W., Kapral, G.J., Grosse-Kunstleve, R.W., et al. (2010). PHENIX: a comprehensive Python-based system for macromolecular structure solution. Acta Crystallogr. D Biol. Crystallogr. *66*, 213–221. https://doi.org/10.1107/s0907444909052925.
59. Pettersen, E.F., Goddard, T.D., Huang, C.C., Meng, E.C., Couch, G.S., Croll, T.I., Morris, J.H., and Ferrin, T.E. (2021). UCSF ChimeraX: structure visualization for researchers, educators, and developers. Protein Sci. *30*, 70–82. https://doi.org/10.1002/pro.3943.
60. Zheng, S.Q., Palovcak, E., Armache, J.P., Verba, K.A., Cheng, Y., and Agard, D.A. (2017). MotionCor2: anisotropic correction of beam-induced motion for improved cryo-electron microscopy. Nat. Methods *14*, 331–332. https://doi.org/10.1038/nmeth.4193.
61. Zhang, K. (2016). Gctf: real-time CTF determination and correction. J. Struct. Biol. *193*, 1–12. https://doi.org/10.1016/j.jsb.2015.11.003.
62. Chen, V.B., Arendall, W.B., 3rd, Headd, J.J., Keedy, D.A., Immormino, R.M., Kapral, G.J., Murray, L.W., Richardson, J.S., and Richardson, D.C. (2010). MolProbity: all-atom structure validation for macromolecular crystallography. Acta Crystallogr. D Biol. Crystallogr. *66*, 12–21. https://doi.org/10.1107/s0907444909042073.

STAR★METHODS

KEY RESOURCES TABLE

REAGENT or RESOURCE	SOURCE	IDENTIFIER
Antibodies		
Mouse monoclonal anti-c-Myc	Takara	Cat# 631206; RRID: AB_2928131
Mouse monoclonal HRP-conjugated anti-β-Tubulin	ABclonal	Cat# AC030; RRID: AB_2769870
Chemicals, peptides, and recombinant proteins		
SIM SF medium	Sino Biological	Cat# MSF1
SMM 293-TI medium	Sino Biological	Cat# M293TI
DMEM medium	Gibco	Cat# 11965092
Fetal bovine serum	Yeasen	Cat# 40130ES76
Fetal bovine serum	Gibco	Cat# 10270-106
n-Dodecyl-β-D-Maltopyranoside (DDM)	Anatrace	Cat# D310
Cholesteryl hemisuccinate (CHS)	Anatrace	Cat# CH210
glyco-diosgenin (GDN)	Anatrace	Cat# GDN101 25 GM
Streptactin Beads 4FF	Smart-Lifesciences	Cat# 2-1201-025
ClonExpress II One Step Cloning Kit	Vazyme	Cat# C112-01
PrimeSTAR HS DNA Polymerase	Takara	Cat# R040A
Lipofectamine 3000	Invitrogen	Cat# L3000015
RIPA lysis buffer	Thermo Fisher Scientific	Cat# 89901
Cisplatin	Sigma	Cat# PHR1624
Cell counting kit-8	Beyotime	Cat# C0039
Deposited data		
Cryo-EM map of $ATP7B_{apo}$	This study	EMDB: EMD-33475
Coordinates of $ATP7B_{apo}$	This study	PDB: 7XUN
Cryo-EM map of $ATP7B_{MBD6\text{-}apo}$	This study	EMDB: EMD-33472
Coordinates of $ATP7B_{MBD6\text{-}apo}$	This study	PDB: 7XUK
Cryo-EM map of $ATP7B_{MBD6\text{-}Cu}$	This study	EMDB: EMD-33474
Coordinates of $ATP7B_{MBD6\text{-}Cu}$	This study	PDB: 7XUM
Cryo-EM map of $ATP7B_{MBD6\text{-}Pt}$	This study	EMDB: EMD-33476
Coordinates of $ATP7B_{MBD6\text{-}Pt}$	This study	PDB: 7XUO
Cryo-EM map of $ATP7B_{AMP\text{-}PNP}$	This study	EMDB: EMD-35628
Coordinates of $ATP7B_{AMP\text{-}PNP}$	This study	PDB: 8IOY
Experimental models: Cell lines		
Spodoptera frugiperda: Sf9	ATCC	Cat# CRL-1711
Human: HEK293T	ATCC	Cat# CRL-3216
Human: HEK293F	Thermo Fisher Scientific	Cat# R79007
Oligonucleotides		
See Table S2 for list of primers for ATP7B mutants	This study	N/A
Recombinant DNA		
Synthesized human *ATP7B* cDNA	GenScript	N/A
pEG BacMam-ATP7B-flagtwinstrep	This study	N/A
pEG BacMam-ATP7B-flagtwinstrep (CPC983-985SPS+D1027A)	This study	N/A
Human *ATP7B* cDNA	This study	GenBank: NM_000053.4
pCMV-Myc-ATP7B	This study	N/A
pCMV-Myc-ATP7B (C575A)	This study	N/A

(*Continued on next page*)

Continued

REAGENT or RESOURCE	SOURCE	IDENTIFIER
pCMV-Myc-ATP7B (C578A)	This study	N/A
pCMV-Myc-ATP7B (M729A)	This study	N/A
pCMV-Myc-ATP7B (C980A)	This study	N/A
pCMV-Myc-ATP7B (C983A)	This study	N/A
pCMV-Myc-ATP7B (C985A)	This study	N/A
pCMV-Myc-ATP7B (D1027A)	This study	N/A
pCMV-Myc-ATP7B (M1359A)	This study	N/A
pCMV-Myc-ATP7B (CPC983-985SPS+D1027A)	This study	N/A
Software and algorithms		
RELION	Scheres[55]	https://www3.mrclmb.cam.ac.uk/relion/
cryoSPARC	Punjani et al.[56]	https://cryosparc.com/
COOT	Emsley et al.[57]	https://www2.mrc-lmb.cam.ac.uk/personal/pemsley/coot/
PHENIX	Adams et al.[58]	https://www.phenix-online.org/
PyMOL	Schrödinger	https://pymol.org/2/
UCSF ChimeraX	Pettersen et al.[59]	https://www.rbvi.ucsf.edu/chimerax/
GraphPad Prism 8.0	GraphPad Software	https://www.graphpad.com/scientific-software/prism/
Other		
R1.2/1.3 300 mesh Au holey carbon grids	Quantifoil	Cat# N1-C14nAu30-01
CF-1.2/1.3-3Au C-flat holey carbon grids	Protochips	Cat# CF313-50-Au
Superose 6, 10/300 GL	GE Healthcare	Cat# 17-5172-01
Vitrobot Mark IV	Thermo Fisher Scientific	https://www.thermofisher.com/cn/zh/home.html
300 kV Titan Krios microscope	Thermo Fisher Scientific	https://www.thermofisher.com/cn/zh/home.html
K2 Summit detector	Gatan	https://www.gatan.com
K3 Summit detector	Gatan	https://www.gatan.com
Falcon4 detector	Thermo Fisher Scientific	https://www.thermofisher.com/cn/zh/home.html

RESOURCE AVAILABILITY

Lead contact

Further information and requests for resources and reagents should be directed to and will be fulfilled by the Lead Contact, Zhi-Ying Wu (zhiyingwu@zju.edu.cn).

Materials availability

Plasmids generated in this study are available from the lead contact with a completed Materials Transfer Agreement. This study did not generate new unique reagents.

Data and code availability

- Atomic coordinates and EM maps of ATP7B$_{apo}$ (PDB: 7XUN; EMDB: EMD-33475), ATP7B$_{MBD6\text{-}apo}$ (PDB: 7XUK; EMDB: EMD-33472), ATP7B$_{MBD6\text{-}Cu}$ (PDB: 7XUM; EMDB: EMD-33474), ATP7B$_{MBD6\text{-}Pt}$ (PDB: 7XUO; EMDB: EMD-33476) and ATP7B$_{AMP\text{-}PNP}$ (PDB: 8IOY; EMDB: EMD-35628) have been deposited in the Protein DataBank (http://www.rcsb.org) and the Electron Microscopy DataBank (https://www.ebi.ac.uk/pdbe/emdb/). Other data reported in this paper will be shared by the lead contact upon request.
- This paper does not report custom code.
- Any additional information required to reanalyze the data reported in this paper is available from the lead contact upon request.

EXPERIMENTAL MODEL AND SUBJECT DETAILS

Insect cell lines

For generating baculovirus, Sf9 insect cells were cultured in SIM SF medium (Sino Biological) with 2% FBS (Yeasen) at 28°C.

Human cell lines

Recombinant proteins were overexpressed in HEK293F cells. The cells were grown in SMM 293-TI medium (Sino Biological) with 2% FBS (Yeasen) at 37°C under 8% CO_2 and were infected when the cell density reached 4.5–5.0×10^6 cells/mL. For the metal transporting assay, HEK293T cells were cultured in DMEM medium (Gibco) with 10% FBS (Gibco) at 37°C in a 5% CO_2 incubator. Plasmids were transfected when the cell confluency reached 60–70%.

METHOD DETAILS

Protein expression and purification

DNA encoding the human *ATP7B* and *ATOX1* gene was synthesized by GenScript with codon optimized based on replacing rare codons with synonymous codons preferentially used in human for enhancing mRNA stability and protein expression (Figure S8) and cloned into a pEG BacMam expression vector with C-terminal *FLAG* and *Twin-Strep* tandem tags and an N-terminal *10× His* tag, respectively. The C983S, C985S, and D1027A combined mutations of *ATP7B* were generated with PrimeSTAR HS DNA Polymerase (Takara) using primers in Table S2. The expression plasmids were transformed into DH10Bac *E.coli* cells for bacmid production, and then the bacmids were used to transfect Sf9 cells with X-tremeGENE 9 DNA Transfection Reagent (Roche) for baculovirus production. The P3 baculovirus was used to infect HEK293F cells at a volume ratio of 1:10, supplemented with 10 mM sodium butyrate to boost protein expression. The mutant ATP7B was heterologously expressed alone or co-expressed with ATOX1 at a virus volume ratio of 1:2. Cells were cultured at 37°C for 48 h and then harvested by centrifugation at 3000× g.

The cell pellet was resuspended in buffer A (50 mM HEPES-NaOH pH 7.4, 150 mM NaCl) supplemented with a protease inhibitor cocktail (2 μg/mL DNase I, 0.5 μg/mL pepstatin, 2 μg/mL leupeptin, 1 μg/mL aprotinin, and 1 mM phenylmethylsulfonyl fluoride) and homogenized by sonication on ice. The ATP7B protein was extracted with 2% (w/v) n-Dodecyl-β-D-Maltopyranoside (DDM, Anatrace) and 0.4% (w/v) cholesteryl hemisuccinate (CHS, Anatrace) by gentle agitation for 2 h at 4°C. The supernatant was collected after centrifugation at 46,000× g for 1 h at 4°C and then incubated with Streptactin Beads 4FF (Smart-Lifesciences) at 4°C for 2 h. The collected resin was rinsed with buffer B (buffer A + 0.025% DDM + 0.005% CHS) for 6-column volumes. The detergent was then changed to glyco-diosgenin (GDN, Anatrace), and the resin was washed with buffer C (buffer A + 0.06% GDN) for 9-column volumes. ATP7B protein was eluted with 10 mM desthiobiotin in buffer C. The protein sample was concentrated and further purified by size-exclusion chromatography with a Superose 6 10/300 GL column (GE Healthcare) equilibrated with buffer C (10 mM DTT was supplemented for ATP7B-ATOX1 complex sample). The protein peak fractions were pooled and concentrated to 7–9 mg/mL for cryo-EM analysis. The band corresponding to ATOX1 on the SDS-PAGE gel of purified ATP7B-ATOX1 complex was weak and identified as indeed ATOX1 protein using mass spectrometry (MS) analysis by Applied Protein Technology (Shanghai) Co., Ltd (Table S3). We have tried to enhance the binding of ATP7B and ATOX1 by adding copper ions during the expression and purification procedure, but failed to obtain a homogeneous protein sample.

Cryo-EM sample preparation and data acquisition

For the Cu^+ or Pt-bound sample, the ATP7B-ATOX1 complex sample was incubated with 300 μM $CuCl_2$ or cisplatin on ice for 1 h prior to the grid preparation. 3 μL aliquots of protein samples were applied onto glow-discharged holey carbon grids (Quantifoil Au R1.2/1.3, 300 mesh), which were blotted for 4.5 s under 100% humidity at 4°C before being plunged into liquid ethane using a Mark IV Vitrobot (Thermo Fisher Scientific). For the AMP-PNP-bound sample, the ATP7B protein was concentrated to 26 mg/mL and incubated with 2 mM AMP-PNP and 5 mM $MgCl_2$ on ice for 1 h. 3 μL aliquots of protein samples were applied onto glow-discharged C-flat holey carbon grids (Protochips CF-1.2/1.3-3Au), which were blotted for 8 s under 100% humidity at 4°C before being plunged into liquid ethane using a Mark IV Vitrobot.

The cryo-EM data of ATP7B apo state and ATP7B-ATOX1 complex apo state were collected at the Center of Cryo-Electron Microscopy at Zhejiang University. Grids were loaded onto a Titan Krios microscope (Thermo Fisher Scientific) operated at 300 kV with a K2 Summit direct electron detector (Gatan). SerialEM software was used for automated data collection following standard procedures. A calibrated magnification of 49,310× was used for imaging, yielding a pixel size of 1.014 Å on images. The defocus range was set from −1.1 to −1.3 μm. Data were dose-fractionated to 40 frames with a dose rate of 8 e^-/pixel/s and a total exposure time of 8 s, corresponding to a total dose of about 62 $e^-/Å^2$.

The cryo-EM data of ATP7B-ATOX1 complex Cu^+-bound state and Pt-bound state were collected at the Center of Cryo-Electron Microscopy at Hubei University. Grids were loaded onto a Titan Krios microscope (Thermo Fisher Scientific) operated at 300 kV with a K3 Summit direct electron detector (Gatan). EPU software was used for automated data collection following standard procedures. A calibrated magnification of 105,000× was used for imaging, yielding a pixel size of 0.4255 Å on images. The defocus range was set from −1.0 to −1.5 μm. Data were dose-fractionated to 40 frames with a dose rate of 15.66 e^-/pixel/s and a total exposure time of 2.5 s, corresponding to a total dose of about 54 $e^-/Å^2$.

The cryo-EM data of ATP7B AMP-PNP-bound state was collected at the Center of Cryo-Electron Microscopy at Zhejiang University. Micrographs were acquired on the Titan Krios microscope (Thermo Fisher Scientific) operated at 300 kV equipped with the Selectris energy filter and Falcon4 detector (Thermo Fisher Scientific). EPU software was used for automated data collection according to standard procedures. A calibrated magnification of 140,000× was used for imaging, yielding a pixel size of 0.93 Å on images. The defocus range was set from -0.8 to -1.6 μm. Each micrograph was dose-fractionated to 40 frames under a dose rate of 7.49 e^-/pixel/s, with a total exposure time of 6 s, resulting in a total dose of about 52 e^-/Å^2.

Image processing

The motion correction was performed using the MotionCorr2 program,[60] and the CTF parameters of the micrographs were estimated using the GCTF program.[61] All subsequent steps of image processing were conducted with RELION and cryoSPARC.[55,56]

For the data of ATP7B$_{apo}$, about 1000 particles were manually picked from the micrographs for 2D classification initially. Several representative 2D class averages of ATP7B in different orientations were selected as templates for automated particle picking. The auto-picked 3,769,178 particles from the 4,742 micrographs were extracted with a binning factor of 3 and were subjected to a 2D classification. A total of 1,326,804 particles were selected for two rounds of 3D classification using the human ATP7B model predicted by AlphaFold2 as the reference. After the second round of 3D classification, 338,254 particles from one 3D class were selected for 3D reconstruction, yielding a 3.4 Å resolution map after 3D refinement with C1 symmetry and particle polishing (Figures S2A–S2F). For the data of ATP7B$_{MBD6\text{-}apo}$, ATP7B$_{MBD6\text{-}Cu}$, ATP7B$_{MBD6\text{-}Pt}$ and ATP7B$_{AMP\text{-}PNP}$, data processing was performed following similar procedures (Figures S2G–S2L, and S3). The resolutions were estimated by applying a soft mask around the protein density and the gold-standard Fourier shell correlation (FSC) was set as 0.143 (Figures S2E, S2K, S3D, S3I and S3N). RELION was used to calculate the local resolution.

Model building, refinement, and validation

De novo atomic model building was carried out in Coot[57] based on the 3.4 Å resolution map of ATP7B$_{apo}$. The assignment of amino acid residues was achieved based on the clearly defined density for bulky residues (Phe, Trp, Tyr, and Arg) and AlphaFold2 prediction model of human ATP7B was used as a reference. Models were refined against summed maps using phenix.real_space_refine,[58] with secondary structure restraints and non-crystallography symmetry applied. The initial EM density map allowed us to construct an ATP7B model containing residues 637–1115 and 1144–1405. The same procedure was performed for ATP7B$_{MBD6\text{-}apo}$ and the model containing residues 562–1115 and 1144–1405 was constructed. The ATP7B$_{MBD6\text{-}apo}$ model works as a reference for building models of ATP7B$_{MBD6\text{-}Cu}$, ATP7B$_{MBD6\text{-}Pt}$ and ATP7B$_{AMP\text{-}PNP}$. The statistics for the models' geometries were generated using MolProbity[62] (Table S1). All the structure figures were prepared in PyMoL (The PyMOL Molecular Graphics System, Version 1.8 Schrödinger, LLC.) or ChimeraX.[59]

Mutagenesis, cell culture, and transient transfection

Full-length human *ATP7B* cDNA (GenBank: NM_000053.4) was cloned into pCMV-Myc vector using ClonExpress II One Step Cloning Kit (Vazyme). Eight single-site missense mutations (C575A, C578A, M729A, C980A, C983A, C985A, D1027A, and M1359A) and one triple-site missense mutation (CPC983-985SPS along with D1027A) of *ATP7B* were made using PrimeSTAR HS DNA Polymerase (Takara) and all were confirmed by sequencing. The primers used were listed in Table S2.

HEK293T cells were seeded the day before transfection and cultured at 37°C. Transient transfection of pCMV-Myc vector, wild type (WT) pCMV-Myc-ATP7B, and mutant pCMV-Myc-ATP7B was conducted with lipofectamine 3000 (Invitrogen) following the manufacturer's instructions for the experiments of western blotting and metal transport assay.

Western blotting

HEK293T cells were seeded in 12 well plates. After 48 h of transfection, cells were treated with RIPA lysis buffer (Thermo Fisher Scientific) containing 1 mM phenylmethylsulfonyl fluoride and harvested. After centrifugation at 12,000× g for 20 min at 4°C, supernatant was collected and ran on 4 to 12% Bis-Tris gradient gels (GenScript). Proteins were then transferred to 0.22 μm polyvinylidene difluoride membranes. Membranes were blocked with 5% skim milk in TBS plus 0.1% Tween 20 for 2 h at room temperature, and then incubated with primary antibodies overnight at 4°C and the corresponding secondary antibody conjugated with HRP for 1 h at room temperature. The primary antibodies mouse anti c-Myc (1:1000, Takara, 631206) and HRP-conjugated β-Tubulin (1:5000, ABclonal, AC030) were used. Immunodetection was done through a Bio-Rad gel documentation system.

Cell viability assay

HEK293T cells were seeded in 96 well plates in replicate wells. After 36 h of transfection, cells were treated with 1 mM $CuCl_2$ or 100 μM cisplatin (sigma) for 24 h. Cells without transfection and metal treatment were cultured for the same periods of time, which were used as the control. Cell counting kit-8 (CCK-8, Beyotime) was used to quantitatively evaluate metal induced cell death by measuring the conversion of WST-8 to formazan by dehydrogenases in the intact mitochondria of living cells. 10 μL CCK-8 reagent in 100 μL DMEM was added into each well of cell cultures as a working solution and incubated for 1 h at 37°C prior to the readings. The working solution was used as the blank. The absorbance of the formed formazan dye was recorded by a spectrophotometer at a wavelength of 450 nm. The average blank OD value was calculated and subtracted from the measured sample OD value. Cell viability was expressed as a percentage of the OD value relative to that of the control.

Intracellular copper and cisplatin accumulation

HEK293T cells were seeded in 12 well plates. After 24 h of transfection, cells were treated with 500 μM $CuCl_2$ or 100 μM cisplatin for 24 h. Cells were collected in tubes and fixed with 4% paraformaldehyde. Samples were mixed with 5 mL concentrated HNO_3 in the digestion vessels and then the vessels were transferred to the Mars6 microwave digestion system (CEM) to get decomposed following the digestion procedure. Afterward, the vessels were taken out and 2 mL distilled deionized water was used to wash the inner covers and then incorporated into the vessels. The residual acid was removed through an acid-driven processor until the solution became transparent. The contents were totally transferred into a tube and finally diluted with distilled deionized water to 10 mL for analysis. Copper or platinum amount in samples was quantified by inductively coupled plasma mass spectrometry (ICP-MS) with an iCAP RQ ICP-MS instrument (Thermo Fisher Scientific) at the Analytical Facility at Feed Science Institute of Zhejiang University. The measurement was performed with matrix-matched standards and element Re was used as the internal standard. Cells without transfection and metal treatment disposed following all steps of samples were used as the blank. The average blank value was calculated and subtracted from the measured sample value. The content of copper or platinum was presented as μg/g.

QUANTIFICATION AND STATISTICAL ANALYSIS

Data of cell viability and metal content were expressed as mean ± SD and Student's t test or Welch's t test between WT and the other group was performed for statistical analysis using GraphPad Prism 8.0 (GraphPad Software). The value of $p < 0.05$ was considered as statistically significant.